AGU PUBLICATIONS

Journal of Advances in Modeling Earth Systems

RESEARCH ARTICLE

10.1002/2017MS000926

Key Points:
- The column mass change with the local compensation is more sensitive to the change of the resolution than the dynamic compensation
- The piggybacking experiment untangles the effects of the local compensation from coupling with tropical cyclone dynamics
- The local compensation concentrates vertical exchange of dry static energy and moisture and induces secondary circulation and other effects

Supporting Information:
- Supporting Information S1
- Data Set S1
- Data Set S2
- Data Set S3
- Data Set S4
- Data Set S5
- Data Set S6
- Data Set S7
- Data Set S8
- Data Set S9
- Data Set S10
- Data Set S11
- Data Set S12
- Data Set S13
- Data Set S14

Correspondence to:
H.-C. Kuo,
kuotwa@ntu.edu.tw

Citation:
Ong, H., C.-M. Wu, and H.-C. Kuo (2017), Effects of artificial local compensation of convective mass flux in the cumulus parameterization, *J. Adv. Model. Earth Syst.*, *9*, 1811–1827, doi:10.1002/2017MS000926.

Received 20 JAN 2017
Accepted 19 JUN 2017
Accepted article online 23 JUN 2017
Published online 3 AUG 2017
Corrected 18 NOV 2017

This article was corrected on 18 NOV 2017. See the end of the full text for details

Effects of artificial local compensation of convective mass flux in the cumulus parameterization

Hing Ong[1], Chien-Ming Wu[1], and Hung-Chi Kuo[1]

[1]Department of Atmospheric Sciences, National Taiwan University, Taipei, Taiwan

Abstract In this study, a hybrid mass flux cumulus scheme (HYMACS) is developed for the Weather Research and Forecasting Model (WRF). Idealized experiments are performed to evaluate its effects on tropical cyclone simulations. Classical cumulus schemes assume artificial local compensation of convective mass flux. In contrast, HYMACS treats subgrid-scale mass flux convergence or divergence as parameterized mass sources or sinks. When the mass sources or sinks are introduced to the mass continuity equation in a nonhydrostatic fully compressible model, the model dynamics would resolve the mass-compensating motion, i.e., dynamic compensation of convective mass flux. A hierarchy of experiments is conducted to demonstrate the effects of the artificial local compensation. The results of the mass compensation experiment show that the amplitude of the column mass change with the artificial local compensation is more sensitive to the change of the horizontal resolution between 3 and 27 km than the dynamic compensation. The results of the piggybacking tropical cyclone simulations at 9 km resolution suggest that the artificial local compensation in the Kain-Fritsch scheme (KF) concentrates vertical exchange of dry static energy and moisture and induces secondary circulation, which could lead to sea level pressure decrease and enhanced precipitation. These results indicate that the artificial local compensation at the gray-zone resolution could cause significant effects on tropical cyclone dynamics, so it is important to avoid the artificial local compensation for cumulus parameterization at such resolution.

1. Introduction

Cumulus convection is an essential process in the earth system because it interacts with other important processes, such as dynamical, hydrological, radiative, and boundary layer processes. Thus, representing cumulus convection is a fundamental problem in modeling weather and climate of the earth system. However, one of the major problems in representing cumulus convection in the large-scale models is the lack of a general framework for the cloud model in the cumulus parameterization to have a horizontally nonlocal structure [*Arakawa*, 2004]. When the horizontal resolution reaches the gray-zone resolution at tens of km or finer, the horizontally nonlocal structure should be viewed as a hybrid issue involving subgrid-scale and grid-scale processes [*Arakawa and Wu*, 2013; *Arakawa et al.*, 2011; *Molinari and Dudek*, 1992]. One approach called the unified parameterization adjusts the effects of the cumulus parameterization through diagnosing the convective updraft fraction, and the horizontally nonlocal structure of convective systems is passed from the subgrid-scale processes to the grid-scale ones when the convective updraft fraction increases [*Arakawa and Wu*, 2013; *Wu and Arakawa*, 2014]. Nevertheless, other approaches could be parameterizing the relative subgrid-scale vertical transport with respect to the grid-scale one [*Park*, 2014] or directly replacing the cumulus parameterization with a cloud-resolving model [*Grabowski*, 2001; *Grabowski and Smolarkiewicz*, 1999]. In this study, we focus on improving the cloud model in the cumulus parameterization as a basis for the unified parameterization.

The cloud model in the cumulus parameterization usually includes convective drafts and their environment. At the gray-zone resolution, the hybrid approach treats convective drafts as subgrid-scale processes but permits the environment to be horizontally nonlocal [*Kain*, 2004; *Kain and Fritsch*, 1990, 1993; *Kreitzberg and Perkey*, 1977; *Kuell and Bott*, 2008; *Kuell et al.*, 2007; *Molinari and Dudek*, 1992]. There have been two stages of the development of the hybrid approach. In the first stage, *Kreitzberg and Perkey* [1977] developed a hybrid scheme for allowing nonlocal precipitation of convective-generated hydrometeors. It deals with subgrid-scale hydrometeor flux convergence as subgrid-scale hydrometeor sources, which are introduced

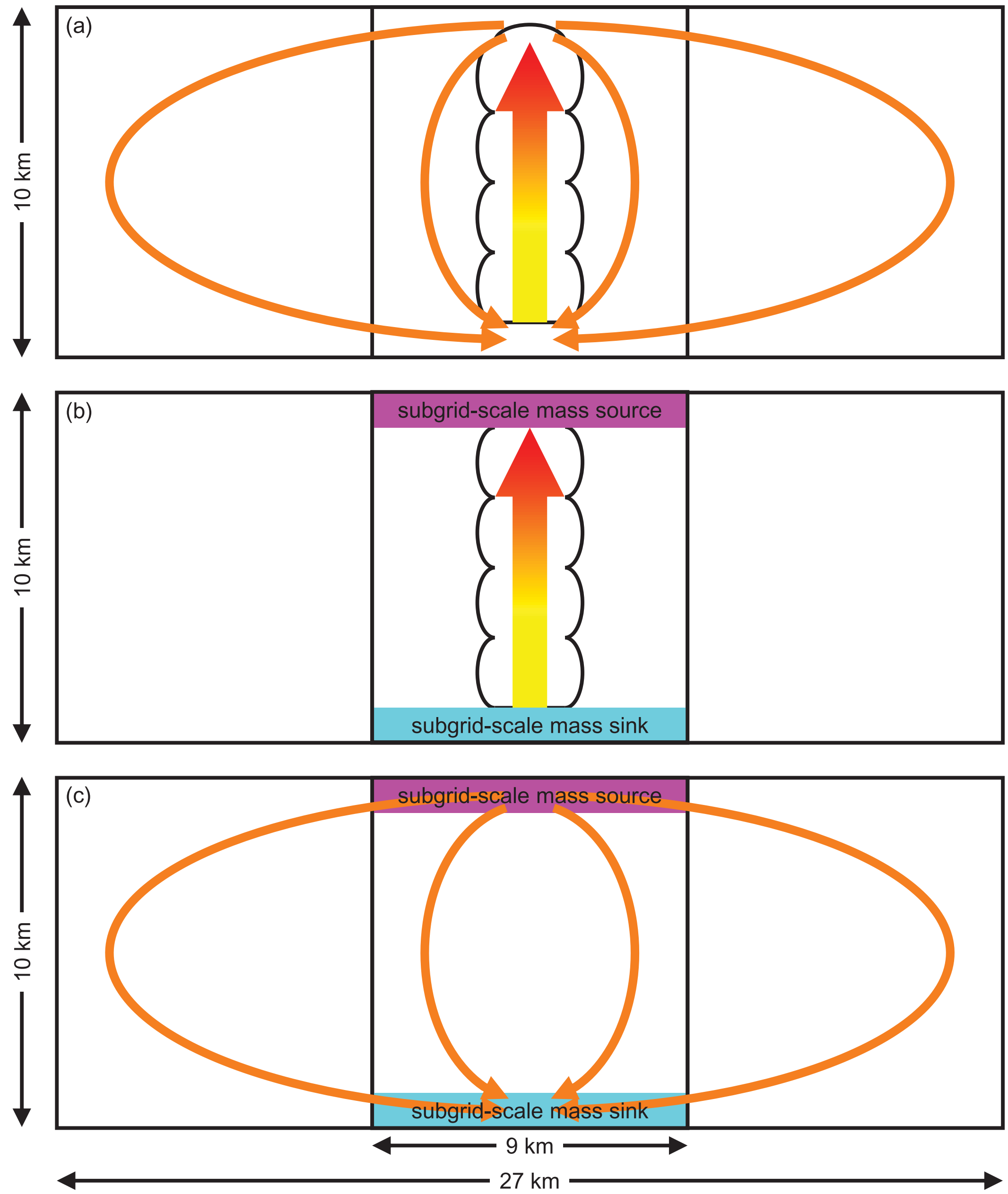

Figure 1. The schematic vertical cross sections for HYMACS are depicted as follows: (a) the scale of a convective updraft and a mass-compensating environment compared with the size of grid columns; (b) how subgrid-scale mass convergence or divergence is treated in a grid column; and (c) how grid-scale dynamics respond to the subgrid-scale mass source and sink.

to the grid-scale hydrometeor equations so that the model dynamics and the microphysics scheme could adjust the precipitation. Combining this approach and the convective available potential energy removal closure [*Fritsch and Chappell*, 1980], the Kain-Fritsch schemes (KF) [*Kain*, 2004; *Kain and Fritsch*, 1990, 1993] have become one of the most popular cumulus schemes in the Weather Research and Forecasting Model (WRF) [*Skamarock et al*., 2008]. In the second stage, *Kuell et al*. [2007] advanced the hybrid approach for permitting nonlocal compensation of convective mass flux, and a scheme using such approach is called a hybrid mass flux cumulus scheme (HYMACS). They suggested that as the increase of the horizontal resolution, the assumption of local compensation of convective mass flux might not be valid as illustrated in an example in Figure 1. In Figure 1a, the cumulus cloud represents a convective updraft, and the orange arrows represent the mass-compensating motion. When the grid size is large (27 km in this figure), the compensating motion occurs within the grid cell. With the increase of the horizontal resolution (9 km), the compensating motion can spread wider than the grid cell. In this case, classical cumulus schemes with the artificial, i.e., humanly contrived, local compensation might overdo their jobs. On the other hand, HYMACS treats subgrid-scale mass flux convergence or divergence as subgrid-scale mass sources or sinks as shown in Figure 1b, where a subgrid-scale convective updraft lifts some air mass from the bottom to the top, making the bottom a mass sink and making the top a mass source. Then, the mass sources and sinks are used in the mass continuity equation in a fully compressible nonhydrostatic model to dynamically adjust the compensating motion, hereafter the dynamic compensation. *Kuell et al*. [2007] performed mass lifting experiments which show that the dynamic compensation could spread horizontally as schematically shown in Figure 1c, where the grid-scale compensating motion is depicted; some of the compensating motion spreads to the adjacent grid cells. Furthermore, HYMACS was tested in various real cases and got realistic results in terms of the spatial distribution of precipitation [*Kuell and Bott*, 2008, 2009]. Nevertheless, a similar approach was tested in *Grell and Freitas* [2014], but the mass compensation is artificially spread to the adjoining grid columns only. On the other hand, classical schemes offset the net subgrid-scale mass flux with the artificial local compensation, heating the air mass instead of lifting it. In comparison to the dynamic compensation, the local compensation should do the same amount of forcing and might further concentrate the forcing, which could enhance the horizontal gradient of the forcing around the grid column. In response, the grid-scale mass fields would be adjusted toward hydrostatic balance by thermal-induced secondary circulation given enough horizontal gradient of the thermal forcing. Note that the local-compensating mass flux is inversely proportional to the area of the grid cell owing to mass conservation. Thus, given the subgrid-scale convective draft, it is hypothesized that the grid-scale transient response, e.g., the column mass change, with the local compensation might be more sensitive to the change of the horizontal resolution than that with the dynamic compensation. If this is true, HYMACS might be a proper first step toward the unified parameterization because it can be adapted from a classical scheme without introducing any new parameter as formulated in Appendix section A1 through section A3. In this study, following *Kuell et al*. [2007], a mass compensation experiment with WRF further compares the dynamic compensation with the local one in terms of the sensitivity to the change of the horizontal resolution from 3 km to 27 km while the forcing is controlled by prescribed conditions.

With the increase of computer resources, the horizontal resolution of fully compressible nonhydrostatic global models [*Gassmann*, 2013; *Miyakawa et al*., 2014; *Skamarock et al*., 2012] reaches the gray-zone resolution at tens of km or finer, even within 1 km, and the performance of tropical cyclone simulations is important for such models. For example, *Yamada et al*. [2010] projected the future changes in tropical cyclone activities with the Nonhydrostatic Icosahedral Atmospheric Model (NICAM) at 14 km resolution without any cumulus parameterization, but *Emanuel et al*. [2010] pointed out that the horizontal resolution was too coarse to simulate intense tropical cyclones, causing a truncation error of the intensity spectrum. Moreover, a wide range of horizontal resolution from 1 km to 9 km is tested for real tropical cyclone cases [*Davis and Bosart*, 2002; *Gentry and Lackmann*, 2010; *Sun et al*., 2013]. Their results suggested that the simulations at 3 km resolution without any cumulus parameterization agree best with observed intensification, and those with finer resolution capture more convective drafts. *Sun et al*. [2013] further pointed out that advances in current cumulus schemes could be important to tropical cyclone simulation. For instance, previous studies [*Davis and Bosart*, 2002; *Singh and Mandal*, 2014; *Srinivas et al*., 2007; *Sun et al*., 2013] suggested that the minimum sea level pressure of simulated tropical cyclones with KF scheme at about 9 km resolution has a low bias which could reach 30 hPa. In this paper, the role of the local compensation in the simulated tropical cyclone is assessed through analyzing the transient effects of removing the local compensation. Accordingly, we adapt KF scheme into a HYMACS (HY) where the dynamic compensation is used instead of the local compensation while the trigger function and the algorithm diagnosing the subgrid-scale convective drafts remain unchanged. The detailed formulation of HY and KF for WRF is in Appendix section A1 through section A4, and additional descriptions on the grid-scale response to each scheme are in Appendix section A5. Note that the subgrid-scale convective drafts and the mass-compensating motion exchange mass vertically. Given the subgrid-scale convective drafts, the dynamic compensation partially spreads to adjacent grid cells, but the local compensation is locally concentrated. Thus, it is hypothesized that the local compensation concentrates vertical exchange of air mass, causing a concentrated vertical exchange of dry static energy and moisture. The grid-scale response to the exchange might be shifted away from where the subgrid-scale forcing occurs owing to the secondary circulation of the tropical cyclone [*Houze*, 2010;

Rotunno and Emanuel, 1987]. Also, the secondary circulation in response to the subgrid-scale thermal forcing might be inhibited in regions with high inertial stability, which enhances the grid-scale thermal response [*Rozoff et al*., 2012; *Schubert and Hack*, 1982] and might lead to changes in sea level pressure or precipitation. To this end, a piggybacking experiment [*Grabowski*, 2015] of idealized tropical cyclone simulations with WRF at 9 km resolution untangles the effects of the local compensation from coupling with tropical cyclone dynamics because KF and HY are compared while the tropical cyclone is controlled by driving simulations.

The mass compensation experiment is presented in section 2. The effects of artificial local compensation in the piggybacking experiment is presented in section 3. Summaries and discussions are presented in section 4.

2. Mass Compensation Experiment

2.1. Design

The mass compensation experiment aims to test the sensitivity of mass compensation processes to the change of the horizontal resolution. Following the mass lifting experiments in *Kuell et al*. [2007], in which the dynamic compensation is tested, this experiment further compares the dynamic compensation with the local compensation with horizontal resolution at 3, 9, and 27 km. Accordingly, there are six sensitivity simulations in this section as follows: L3, L9, L27, D3, D9, and D27, where L denotes the local compensation, and D denotes the dynamic compensation.

To compare the local compensation and the dynamic compensation, a plume model with a prescribed convective updraft is used instead of the plume models in KF. The prescribed updraft is designed to mimic Figure 1b; it lifts air mass in the active column at the middle of the domain from the bottom to 12.5 km height at an arbitrary constant mass lifting rate. The potential temperature of the lifted air mass is set to be the same as that of the environment. Physical parameterization schemes other than the cumulus scheme, including microphysics, planetary boundary layer, surface layer, and radiation, are turned off. Since the mass lifting rate is constant, the sensitivity of the results to the change of the horizontal resolution could only be caused by the mass compensation processes; either the dynamic compensation or the local compensation.

These simulations are conducted with WRF version 3.7.1 using the nonhydrostatic fully compressible model dynamics. The vertical grid spacing is about 1.25 km. The model is integrated for 27 min. Single domain with size equal to 945 km $\times$ 945 km $\times$ 25 km is used. The lateral boundary conditions are periodic. Rayleigh damping is used within the uppermost 5 km. Coriolis parameter is zero. The initial conditions are motionless, horizontally homogeneous, and vertically stratified with the mean hurricane season sounding for the West Indies area [*Jordan*, 1958]. With the increase of the arbitrary mass lifting rate from 10^6 kg s^{-1} to 10^8 kg s^{-1}, the amplitude of the column mass change grows linearly. If the rate is larger than 4×10^7 kg s^{-1}, the model will be unstable at 3 km resolution. In this paper, only the results with the mass lifting rate at 4×10^7 kg s^{-1} are shown.

2.2. Results

To evaluate the resolution dependence of the local compensation verses the dynamic compensation, the temporal evolutions of the column mass change are analyzed. The results are averaged to 27 km resolution to avoid spatial sampling problem. The results of D3, D9, and D27 are comparable with the results of the mass lifting experiments in *Kuell et al*. [2007] in terms of the spatial structures of the momentum fields, including inflow in the layer with a mass sink, outflow in the layer with a mass source, and gravity waves radiating from the active column.

The local-compensating downward mass flux is inversely proportional to the area of the grid cell, so the amplitude of transient warming accompanied with column mass reducing with the local compensation should be larger at finer horizontal resolution. Also, the local compensation is artificially concentrated, so the amplitude of the column mass change with it should be more significant than that with the dynamic compensation. In Figure 2, all the temporal evolutions of the column mass change are decreasing and oscillating, which is relevant to external gravity waves. The decrease is more significant with the local compensation than the dynamic compensation for each resolution. Moreover, for a scheme, the difference between

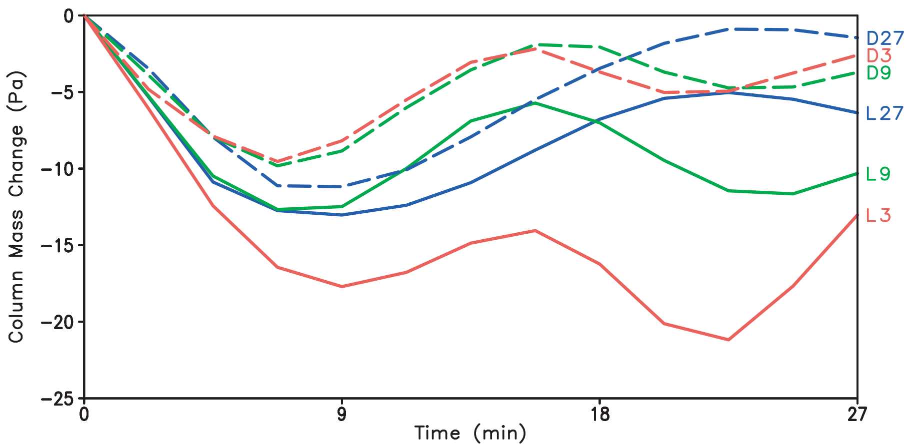

Figure 2. The temporal evolutions of the column mass change in the active column in the mass compensation experiment. L denotes the local compensation, and D denotes the dynamic compensation. The horizontal resolution of 3, 9, and 27 km are used. The results are averaged to 27 km resolution to avoid spatial sampling problem.

the amplitude of the oscillation at various resolution implies the sensitivity to the change of the horizontal resolution. Though there are various phases of the oscillation, the amplitude at a certain phase could be a proxy for that of the oscillation. For example, at the crest, the difference between the amplitude of L27 and L3 is seven times larger than that of D27 and D3, and this could be generally applied to other phases. However, the frequency of the oscillation is independent of the change of scheme but is dependent on the change of the horizontal resolution; the finer the horizontal resolution, the larger the frequency. This could be attributed to the proportionality of the frequency to the horizontal wave number. Comparing finer resolution with coarser one, the active column is narrower, so the horizontal wave number of the triggered waves is larger. Note that the waves with high wave number and high frequency at 3 km or 9 km resolution are averaged out in Figure 2.

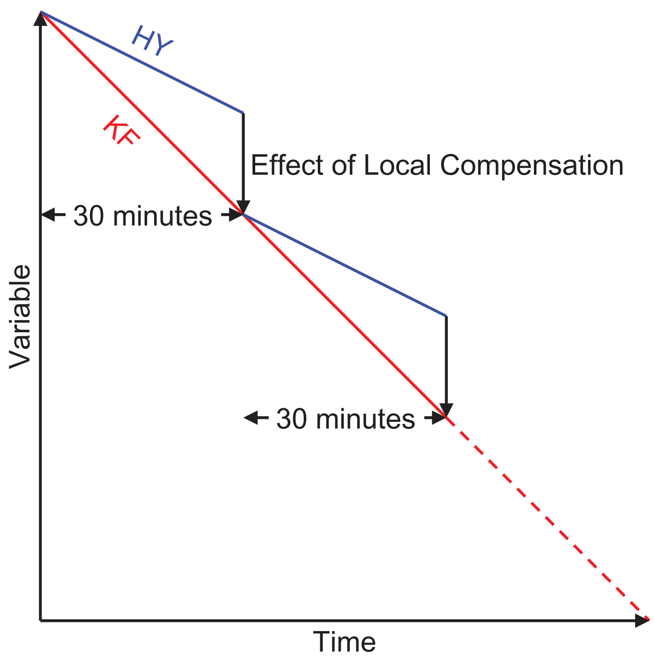

Figure 3. The schematic diagram for the piggybacking experiment. The driving simulation (red) is run with KF, with the local compensation, and the piggybacking (blue) is restarted with HY, with the dynamic compensation, every 30 min, as if HY piggybacks KF. Subtracting HY from KF could be an approximation to the effect of the local compensation.

Accordingly, switching the scheme from the local compensation to the dynamic one reduces the sensitivity of the amplitude of external gravity waves to the horizontal resolution. This could be attributed to the mass conservation with the local compensation; the narrower the grid cell, the stronger the mass-compensating subsidence. However, the switching does not change the dependence of frequency on the horizontal resolution.

3. Piggybacking Experiment

3.1. Design

The piggybacking experiment is designed to untangle the transient effects of the local compensation from coupling with tropical cyclone dynamics. A schematic diagram for the piggybacking approach is presented in Figure 3. In order to examine the effects in various initial conditions, an idealized tropical cyclone simulation is performed with KF for 5 days and is restarted with

HY every 30 min; that is, the initial conditions of the piggybacking simulations with HY are predicted by a driving simulation with KF, as if HY piggybacks KF. To focus on the change in a characteristic time of convective adjustment, a reasonable approximation to the effects of the local compensation could be subtracting the results at end of a 30 min simulation with HY from that with KF. It is required that the primary circulation is controlled by the driving simulation in 30 min of piggybacking simulation, and this is justified in the results. On the other hand, KF piggybacking HY fails because KF is unable to deal with the mass sources or sinks calculated by HY, which remain constant after restarting with KF.

The piggybacking experiment is first conducted at 9 km resolution, and then, various horizontal resolution at 12, 15, 18, and 24 km, are tested to examine the sensitivity of the results to the change of the horizontal resolution. The domain size is 5400 km $\times$ 5400 km $\times$ 25 km. The driving simulations with KF are integrated for 5 days. The initial conditions of the driving simulation are similar to those in the mass compensation experiment, but a hydrostatic and gradient wind balanced hurricane-like vortex [*Rotunno and Emanuel*, 1987] is placed in the middle of the domain. The default settings for idealized tropical cyclone simulation in WRF are used. These include constant Coriolis parameter at 5×10^{-4} s^{-1}, constant sea surface temperature at 28°C, and the following physical parameterization schemes: Kessler microphysics [*Kessler*, 1995], Yonsei University planetary boundary layer [*Hong et al.*, 2006], Monin-Obukhov surface layer [*Beljaars*, 1995; *Dyer and Hicks*, 1970; *Paulson*, 1970; *Webb*, 1970; *Zhang and Anthes*, 1982], and capped Newtonian relaxation [*Rotunno and Emanuel*, 1987].

3.2. Results

First, the overall temporal evolution of the symmetry and intensity in the driving simulation with KF at 9 km resolution is surveyed. With respect to the center of the tropical cyclone, the axisymmetric component of the precipitation is stronger than the asymmetric one after the 48th hr of the simulation. Then, the tropical cyclone rapidly intensifies for 1 day and becomes steady after that. For instance, in the tropical storm (TS) stage from the 48th hr to the 60th hr, the maximum 10 m wind speed enhances from 19.1 m s^{-1} to 30.8 m s^{-1}, and in the typhoon (TY) stage from the 108th hr to the 120th hr, it fluctuates between 49.7 m s^{-1} and 50.0 m s^{-1}. Intervals of 12 hr are short enough so that the temporal averages of all signals discussed later would not be exceeded by the temporal standard deviation in each stage.

Then, the overall spatial distribution of the precipitation in the driving simulation with KF at 9 km resolution is scrutinized. In Figure 4, the horizontal distributions of the subgrid-scale and the total precipitation in the TS and the TY stage in the driving simulation with KF are depicted; the subgrid-scale precipitation is calculated by a cumulus scheme while the total precipitation is the sum of the subgrid-scale one and the grid-scale one calculated by a microphysics scheme. The radius of the maximum total precipitation determines the eyewall of the tropical cyclone. In general, the grid-scale precipitation dominates in the eyewall while the subgrid-scale one spreads from the eyewall to the outside of it. Also, the subgrid-scale precipitation in the TS stage is more than that in the TY stage.

To evaluate the effects of the local compensation, the results of the piggybacking simulation with HY are subtracted from those of the driving simulation with KF. Since the local-compensating downward mass flux is artificially concentrated, it concentrates vertical exchange of dry static energy. This causes the upper air to lose enthalpy and the lower air to gain that, so dipole structures of subgrid-scale specific enthalpy forcing (see Appendix section A5 for detailed calculation) are found in regions with parameterized convective mass flux. In Figure 5, the subgrid-scale specific enthalpy forcing due to the local compensation (KF – HY) is depicted. One forcing dipole is aligned with the subgrid-scale precipitation maximum near the eyewall in each stage, and another one is found near the center in the TY stage; the former is caused by the local compensation of the mass flux of parameterized deep convection, and the latter is caused by that of parameterized shallow convection. Also, the forcing dipole in the deep convection region in the TS stage is stronger than that in the TY stage, which is consistent with the amount of subgrid-scale precipitation.

The subgrid-scale forcing dipoles due to the local compensation lead to grid-scale thermal dipoles, and the secondary circulation of the tropical cyclone [*Houze*, 2010; *Rotunno and Emanuel*, 1987] might transport the thermal dipole away from the subgrid-scale forcing dipole. In Figure 6, thermal dipoles with upper air losing dry static energy and lower air gaining dry static energy are identified. While the thermal dipole near the center in the TY stage is aligned with the forcing dipole there, the thermal dipole near the eyewall shifts upward and outward in each stage. The order of magnitude of the shift is consistent with that of the

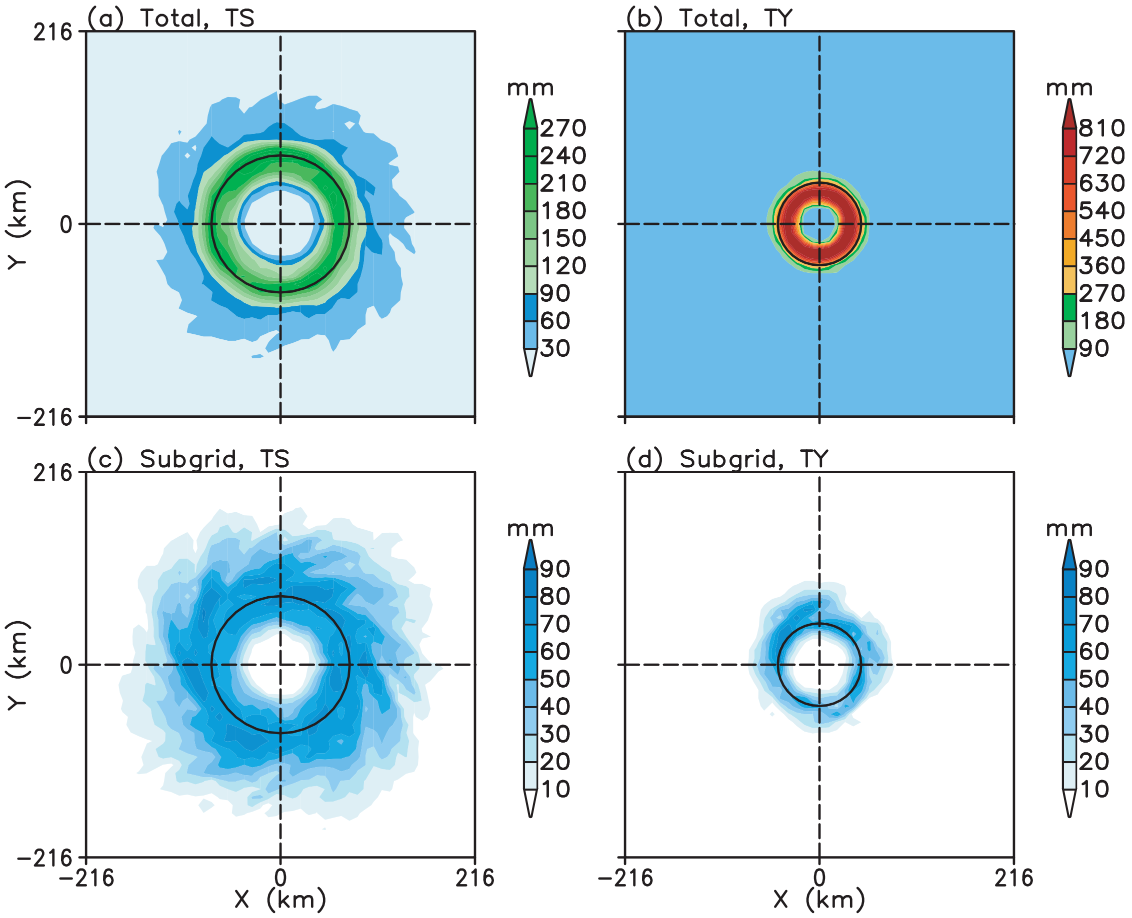

Figure 4. The horizontal distributions in the (left) TS stage and (right) TY stage in the driving simulation in the piggybacking experiment at 9 km resolution of the (top) total precipitation and (bottom) subgrid-scale precipitation. The circles denote the radii of the maximum subgrid-scale precipitation, 76.8 km in the TS stage and 46.2 km in the TY stage.

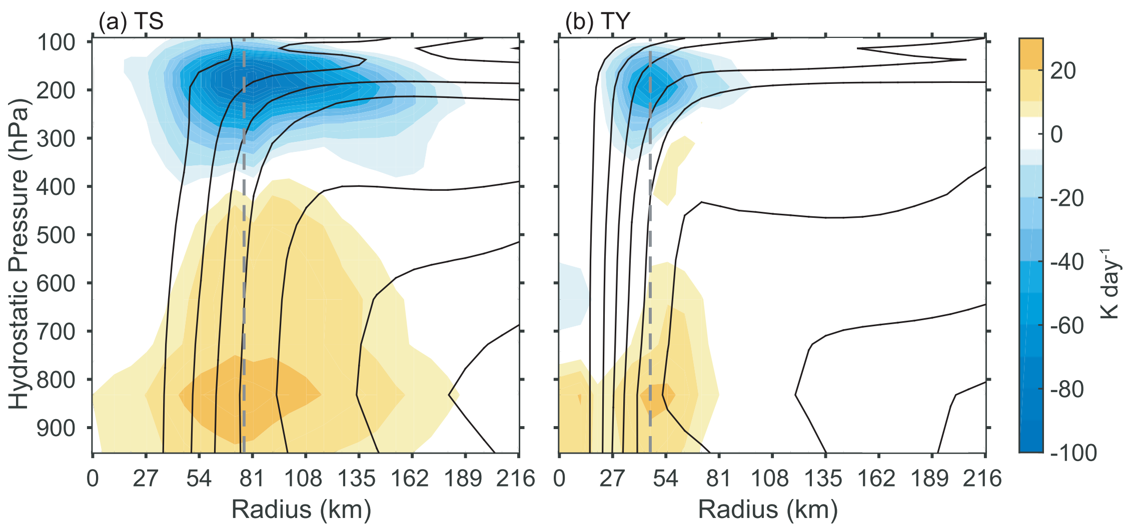

Figure 5. The vertical cross sections in the (left) TS stage and (right) TY stage in the piggybacking experiment at 9 km resolution of the azimuthal and temporal average of the variables in the following: shaded, the subgrid-scale specific enthalpy forcing (rate of heating and work done) due to the local compensation (KF – HY); and contour, the absolute angular momentum (interval: 5×10^5 m^2 s^{-1}) in the driving simulation (KF). The dash lines denote the radii of the maximum subgrid-scale precipitation.

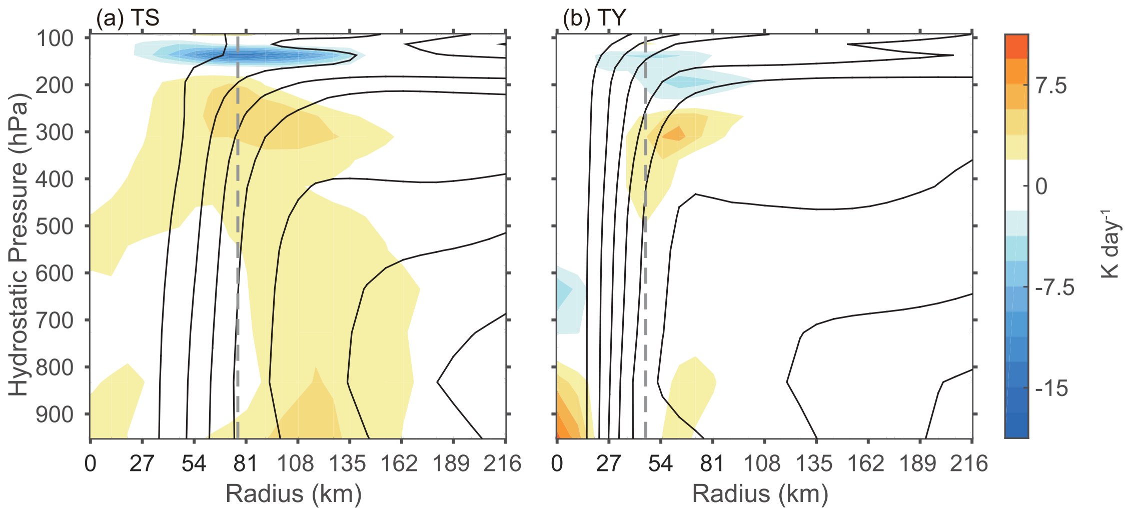

Figure 6. Similar to Figure 5. The colored shades are the specific dry static energy change rate due to the local compensation (KF – HY) in 30 min of piggybacking simulation.

secondary circulation of the tropical cyclone near the eyewall, which is 10^0 m s^{-1} upward and 10^1 m s^{-1} outward. Also, the portion of the grid-scale thermal dipole in response to the subgrid-scale forcing is one half near the center and is one sixth outside of the eyewall. This could be attributed to high inertial stability near the center; the higher the inertial stability, the larger portion of thermal response to a forcing occurs locally [*Rozoff et al*., 2012; *Schubert and Hack*, 1982]. Since the change rate of geopotential is one order smaller than that of specific enthalpy in the results, losing or gaining dry static energy indicates cooling or warming, respectively. In the deep convection regions, the cooling layer is shallow above the tropopause, and there is overall warming in the troposphere.

Similarly, the local-compensating downward mass flux concentrates vertical exchange of moisture. In Figure 7, the water vapor mixing ratio change rate due to the local compensation (KF – HY) is depicted. Moisture dipoles with upper moistening and lower drying are identified. The moisture dipole and the thermal one are opposite because the vertical gradient of moisture and dry static energy are opposite. Also, the moisture dipole lies lower than the corresponding thermal dipole. This might be attributed to the distribution of the gradient; comparing the lower level with the upper, the vertical gradient of moisture is stronger, but that of specific dry static energy is weaker.

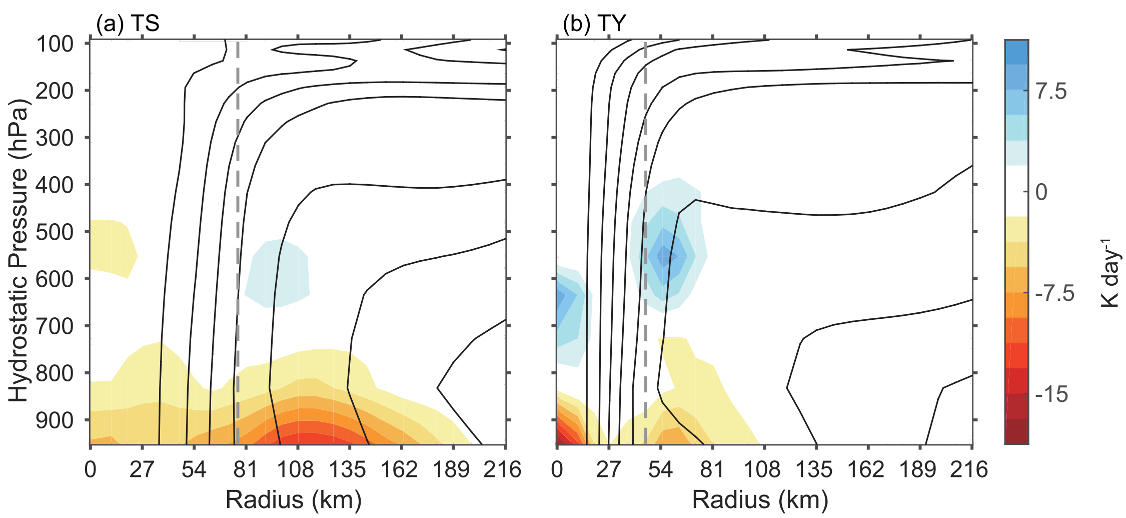

Figure 7. Similar to Figure 5. The colored shades are the water vapor mixing ratio change rate due to the local compensation (KF – HY) in 30 min of piggybacking simulation.

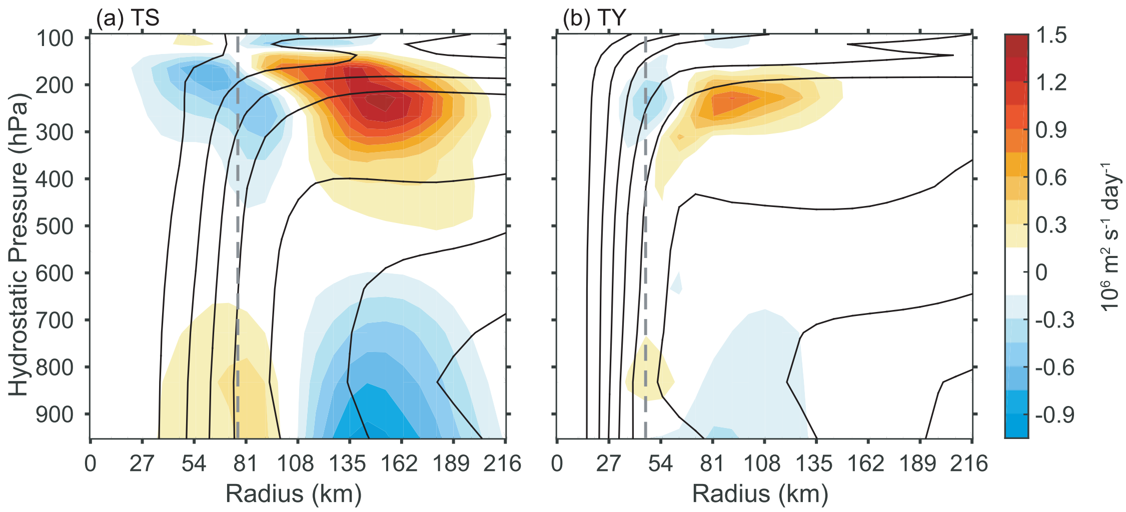

Figure 8. Similar to Figure 5. The colored shades are the radial mass flux change rate due to the local compensation (KF – HY) in 30 min of piggybacking simulation. The radial mass flux is defined as the radial velocity times the radius.

In addition to the dipoles, a region with net warming and net drying whose maximum lies 30 km outside of the radius of maximum subgrid-scale precipitation is identified in the TS stage, which cannot be explained with an exchange. This could be attributed to extra condensation due to the thermal-induced secondary circulation; since the thermal structure changes, secondary circulation with lower convergence and upper divergence in the warming region would be induced. In Figure 8, the radial mass flux change rate due to the local compensation (KF – HY) and the absolute angular momentum in the driving simulation (KF) are depicted. Note that KF in WRF has no subgrid-scale momentum sources or sinks, so the radial mass flux change indicates the thermal-induced secondary circulation. However, since secondary circulation change favors low inertial stability [*Rozoff et al*., 2012; *Schubert and Hack*, 1982], the induced secondary circulation due to the shallow convection near the center is inhibited owing to large inertial stability. Also, the inner branch of the induced secondary circulation near the eyewall is weaker than the outer branch. The induced secondary circulation is accompanied with extra upward motion whose location is consistent with the net warming and drying, and this gives the reason for the extra condensation.

The induced secondary circulation causes other effects, including enhanced precipitation and sea level pressure decrease. In Figures 9a and 9b, the total precipitation change rate due to the local compensation (KF – HY) is depicted. Indeed, the enhanced precipitation is identified in regions with extra upward motion. In Figures 9c and 9d, the sea level pressure decrease effect due to the local compensation (KF – HY) is found in most regions of the tropical cyclone. This could be caused by hydrostatic adjustment, in which pressure layers are thickening in warming regions. Meanwhile, the strong upper-level outflow of the induced secondary circulation reduces the mass inside. The region of the strongest decrease effect is aligned with the maximum of upper divergence of the induced secondary circulation. The decrease effect could reach -9 hPa d^{-1} in the TS stage.

We survey the results at 12, 15, 18, and 24 km resolution after studying those at 9 km resolution. The response of a grid-scale variable under a certain subgrid-scale regime to the change of the horizontal resolution is concerned. Qualitatively, they are all consistent with the results at 9 km. Quantitatively in Table 1, the subgrid-scale processes differ in various resolution; e.g., from 9 km to 18 km, the areal mean subgrid-scale precipitation rate increases, but from 18 km to 24 km, it decreases. Moreover, the effects of the local compensation are also sensitive to the horizontal resolution; e.g., from 9 km to 12 km, the areal mean sea level pressure decrease rate due to the local compensation increases, but from 12 km to 24 km, it decreases. Understanding the sensitivity of subgrid-scale precipitation to the change of the horizontal resolution requires testing a few parameters in diagnosing the subgrid-scale convective drafts in KF, which is beyond the scope of this study. However, combining these variables, the pressure decrease due to the local compensation divided by subgrid-scale precipitation increases monotonically with the horizontal resolution increase. Though the ratio could be more complex than a function of the horizontal resolution, this implies

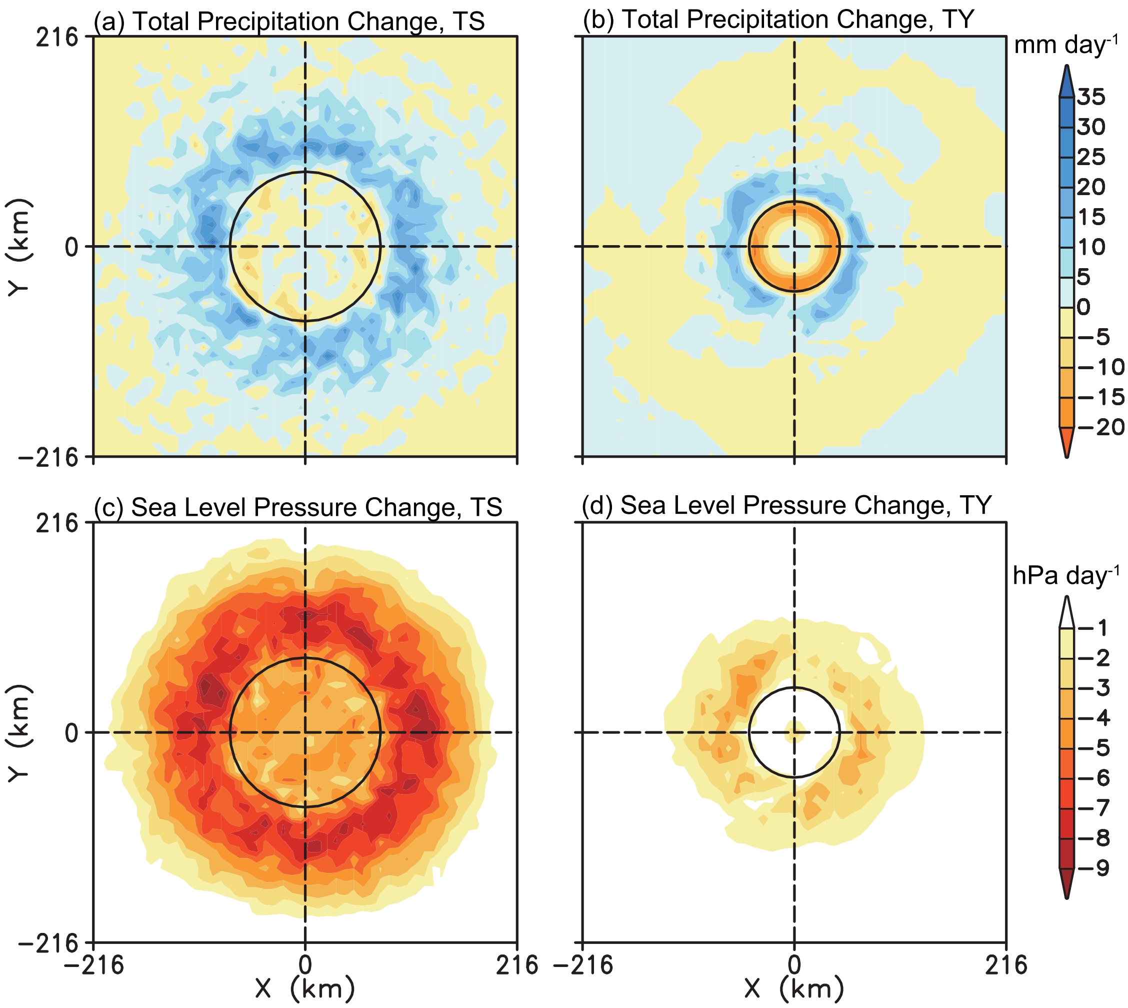

Figure 9. The horizontal cross sections in the (left) TS stage and (right) TY stage in the piggybacking experiment at 9 km resolution of the temporal average of the change rate of the total precipitation (upper) and the sea level pressure (lower) due to the local compensation (KF – HY) in 30 min of piggybacking simulation. The circles denote the radii of the maximum subgrid-scale precipitation.

that pressure decrease due to the local compensation might be larger with finer horizontal resolution if it could be normalized with the subgrid-scale precipitation.

Overall, in comparison to HY, the results of the piggybacking experiment support the hypothesis that KF concentrates vertical exchange of dry static energy and induces secondary circulation. Moreover, the induced secondary circulation could cause other effects including sea level pressure decrease and enhanced precipitation. Furthermore, the significance of those effects is justified by comparing the absolute value of KF – HY with the standard deviation of the natural variability in the simulated tropical cyclone.

Table 1. List of Results at Various Resolution in the Piggybacking Experiment[a]

Resolution (km)	Prec (mm d^{-1})	dP (Pa d^{-1})	dP $Prec^{-1}$ (Pa mm^{-1})
9	20.1	−289	−14.4
12	24.6	−323	−13.1
15	27.3	−278	−10.2
18	28.6	−259	−9.06
24	27.5	−165	−6.01

[a]Prec denotes the areal mean subgrid-scale precipitation rate in the driving simulation with KF in the central 216 km × 216 km square. dP denotes the areal mean sea level pressure change rate due to the local compensation (KF – HY) in the square.

4. Summaries and Discussions

Representing cumulus convection is an essential problem in modeling the earth system to predict weather and climate. A horizontally nonlocal framework for representing subgrid-scale cumulus convection is examined with a hybrid mass flux cumulus scheme (HYMACS) adapted from the Kain-Fritsch scheme (KF). Instead of local compensation of convective mass flux, HYMACS treats subgrid-scale mass flux convergence or divergence as parameterized mass sources or sinks. When the mass sources or sinks are introduced to the mass continuity equation in a nonhydrostatic fully compressible model, the model dynamics would resolve the mass-compensating motion, i.e., the dynamic compensation. With the Weather Research and Forecasting Model (WRF), a hierarchy of idealized experiments is conducted to assess the effects of the local compensation in tropical cyclones.

In the mass compensation experiment, a subgrid-scale updraft is prescribed to evaluate the sensitivity of the column mass change with each mass compensation process to the change of the horizontal resolution between 3 and 27 km. The results indicate that the amplitude of the column mass change with the dynamic compensation is less sensitive to the change of the horizontal resolution than the local compensation. In the piggybacking experiment, by subtracting the results with the hybrid mass flux KF (HY) from those with KF, the transient effects of the local compensation in a characteristic time of convective adjustment are untangled from coupling with tropical cyclone dynamics at 9 km resolution. The results support the hypothesis that the local compensation concentrates vertical exchange of dry static energy and moisture and could lead to sea level pressure decrease and enhanced precipitation by thermal-induced secondary circulation. Comparing the tropical storm (TS) stage with the typhoon (TY) stage, these effects are stronger, which could be attributed to more subgrid-scale precipitation. Also, the induced secondary circulation is weaker in regions with higher inertial stability. These results indicate that the artificial local compensation at the gray-zone resolution could cause significant effects on tropical cyclone dynamics, so it is important to avoid the artificial local compensation for cumulus parameterization at such resolution.

A remaining issue is whether HY could reduce the low bias of minimum sea level pressure of simulated tropical cyclone with KF at 9 km resolution. A preliminary cumulus-cyclone-coupled experiment uses an explicit scheme without cumulus parameterization at 3 km resolution (NO3) as a reference to compare with the simulation at 9 km resolution with KF (KF9) and HY (HY9). The design follows the piggybacking experiment, but each simulation is integrated for 5 days. The results after 2 day spin-up are depicted in Figure 10. After 3 days of intensification, the minimum sea level pressure in KF9 is 30 hPa lower than that in NO3, but that in HY9 is 10 hPa higher than that in KF9. The results suggest that HY could reduce the low bias of minimum sea level pressure at 9 km resolution. However, the following problems should be considered in the future. First, the effects of local compensation are transient and might not affect tropical cyclone development owing to the nonlinear interaction between the cyclone-scale and the cumulus-scale processes. Second, both schemes assume $\sigma \ll 1$, which might overestimate subgrid-scale mass flux at 9 km resolution. Third, neither scheme considers subgrid-scale momentum sources or sinks which might decelerate the primary circulation. Real-case studies are needed to verify the conjecture.

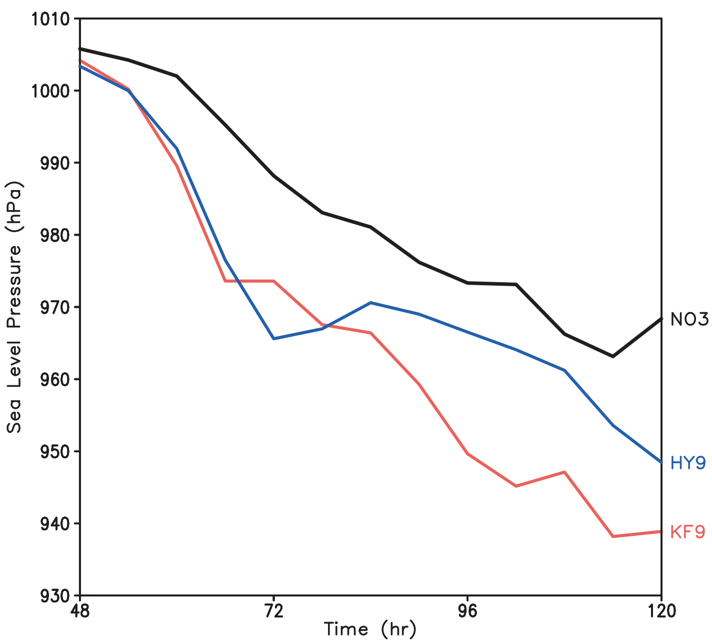

Figure 10. The temporal evolutions of the minimum sea level pressure in the cumulus-cyclone-coupled experiment after 2 day spin-up. NO3 is the control simulation, at 3 km resolution with the explicit scheme, and KF9 and HY9 are the sensitivity simulations, at 9 km resolution with KF and HY, respectively.

For the future development of the unified parameterization, a hierarchy of cumulus schemes from particular ones to general ones should be established. According to the scheme formulation in Appendix section A1 through section A3, by eliminating the assumptions one by one, the hierarchy with six levels could be built as shown in Figure 11. Level

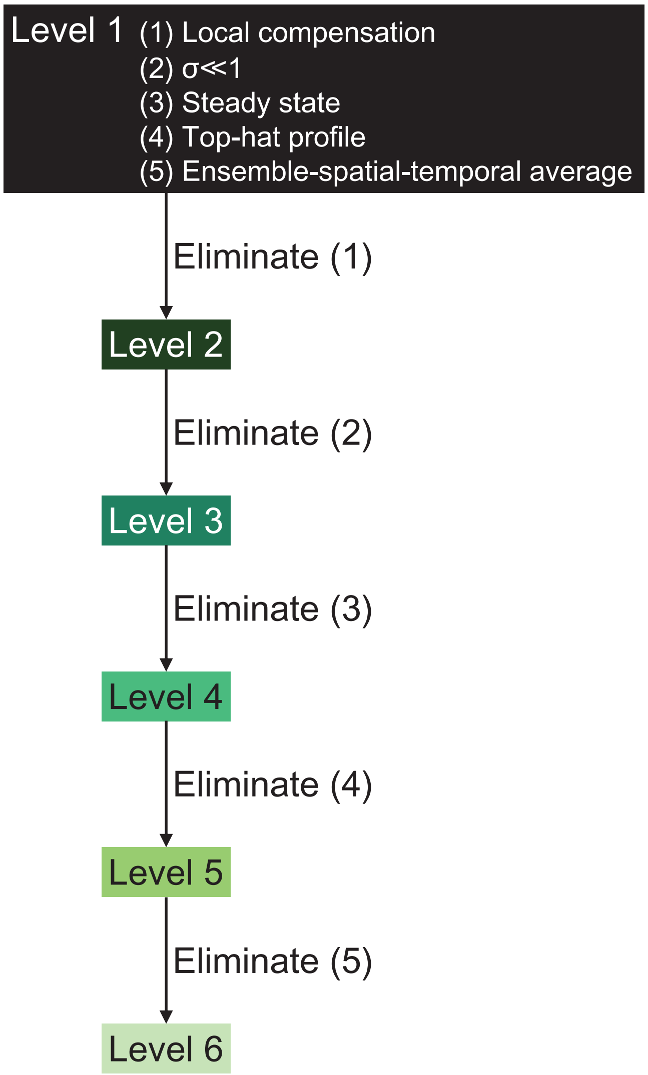

Figure 11. The flow diagram of the hierarchy of cumulus schemes. The hierarchy could be built by eliminating the five assumptions one by one.

1 is conventional cumulus schemes where the following five assumptions are used: the local compensation, the $\sigma \ll 1$, the steady-state plume, the top-hat profile, and the ensemble-spatial-temporal average. Level 2 is HYMACS, where the local compensation is replaced by the dynamic compensation so that the mass-compensating motion is resolved. In Level 3, the $\sigma \ll 1$ is eliminated by parameterizing σ so that the convective drafts could be partially resolved. In Level 4, the steady-state plume is eliminated by prognostic closures, so the convective drafts could interact with the grid-scale changes which are faster than the convective turnover time. In Level 5, a more complex profile than the top-hat profile is used, so the structure within the convective drafts or within the environment could be considered. In Level 6, the ensemble average is no longer treated as the spatial average in a grid box, so the problem could be considered in a continuous space. Most of the assumptions should be replaced by more sophisticated ones except the local compensation. The unified parameterization should be developed following the hierarchy level by level. Consequently, the next step could be combining HYMACS with σ parameterization [e.g., *Arakawa and Wu*, 2013; *Grell and Freitas*, 2014; *Park*, 2014; *Wu and Arakawa*, 2014; *Zheng et al.*, 2016].

Finally, it should be pointed out that HY by no means fully represents the nature of subgrid-scale cumulus convection. In addition to the five assumptions mentioned above, the trigger function and the algorithm diagnosing the subgrid-scale convective drafts in KF could be affected by increasing the horizontal resolution to the gray zone, e.g., the finer the horizontal resolution, the smaller subgrid-scale mass flux [*Zheng et al.*, 2016]. Also, as mentioned in section 2, the frequency of gravity waves triggered by mass lifting is dependent on the horizontal resolution. Moreover, the physical parameterization schemes used in this study are idealized. However, the experiments designed in this paper are reasonable steps to understanding the effects of artificial local compensation of subgrid-scale convective mass flux.

Appendix A: Scheme Formulation

A1. An Ensemble Average Continuity Equation Set

HY and KF could be formulated from the continuity equation set. The conservation laws of the fluid dynamics are described by a continuity equation set:

$$\frac{\partial \rho\psi}{\partial t} + \nabla \cdot \rho\psi\mathbf{V} = \rho\dot{\psi}, \tag{A1}$$

where the variables are defined as follows: ρ, mass density; ψ, unity or an intensive quantity; $\mathbf{V}$, three-dimensional vector of velocity; and $\dot{\psi}$, total time derivative of ψ. If ψ is unity, three-dimensional vector of velocity, specific entropy, and various specific moisture contents, equation (A1) would be a nonhydrostatic fully compressible continuity equation set composed of the following density as prognostic variables: mass, momentum, entropy, and moisture contents, respectively. With respect to the prognostic variables, equation (A1) means that the local tendency plus the flux density divergence equals to the density of sources or sinks.

Applying ensemble average to equation (A1), we get:

$$\frac{\partial}{\partial t}\left[\overline{\rho\psi}+(\rho\psi)'\right]+\nabla\cdot\left[\overline{\rho\psi}+(\rho\psi)'\right]\left[\overline{\mathbf{V}}+\mathbf{V}'\right]=\left[\overline{\rho}+\rho'\right]\left[\overline{\dot{\psi}}+\dot{\psi}'\right], \tag{A2}$$

where the over bars and the primes denote the ensemble average and the deviation, respectively. Ensemble averaging and rearranging equation (A2), we get:

$$\frac{\partial\overline{\rho\psi}}{\partial t}+\nabla\cdot\overline{\rho\psi}\,\overline{\mathbf{V}}-\overline{\rho}\,\overline{\dot{\psi}}=\overline{\rho'\dot{\psi}'-\nabla\cdot(\rho\psi)'\mathbf{V}'}. \tag{A3}$$

Equation (A3) describes the ensemble average components of the prognostic variables. *The right hand side is the subgrid-scale sources or sinks term* (SSS_ψ). For example, when ψ is unity, the subgrid-scale mass flux convergence or divergence, $\mathrm{SSS}_1=\overline{-\nabla\cdot\rho'\mathbf{V}'}$, is the subgrid-scale mass sources or sinks.

A2. A General Formulation of HYMACS

Since subgrid-scale convective drafts generally penetrate through a grid column, which is a pile of grid boxes, so one-dimensional plume models are usually used to represent the vertical structure of the convective drafts. However, the plume models describe the total of variables, so SSS_ψ must be rewrote into the difference between the total and the ensemble average:

$$\mathrm{SSS}_\psi=\overline{\rho\dot{\psi}-\nabla\cdot\rho\psi\mathbf{V}}-\overline{\overline{\rho}\,\overline{\dot{\psi}}-\nabla\cdot\overline{\rho\psi}\,\overline{\mathbf{V}}}, \tag{A4}$$

where the two terms are to-be-parameterized by the plume models and to-be-resolved by the model dynamics, respectively. By the ensemble-spatial-temporal average approximation, the ensemble average in equation (A4) could be rewrote into spatial average in a grid box:

$$\mathrm{SSS}_\psi\cong\frac{1}{V}\left[\iiint_D\left(\rho\dot{\psi}-\nabla\cdot\rho\psi\mathbf{V}\right)dV'-\iiint_D\left(\overline{\rho}\,\overline{\dot{\psi}}-\nabla\cdot\overline{\rho\psi}\,\overline{\mathbf{V}}\right)dV'\right], \tag{A5}$$

where D and V are the grid box and its volume, respectively.

The plume models are inserted into the first integral in equation (A5) by decomposing the grid box into a few subgrid columns of convective drafts embedded in a subgrid column of environment:

$$\mathrm{SSS}_\psi\cong\frac{1}{V}\sum_i\left[\iiint_{D_i}\left(\rho\dot{\psi}-\nabla\cdot\rho\psi\mathbf{V}\right)dV'+\iiint_{\tilde{D}}\left(\rho\dot{\psi}-\nabla\cdot\rho\psi\mathbf{V}\right)dV'-\iiint_D\left(\overline{\rho}\,\overline{\dot{\psi}}-\nabla\cdot\overline{\rho\psi}\,\overline{\mathbf{V}}\right)dV'\right], \tag{A6}$$

where the subscripts i and the tildes denote the ith subgrid column of convective drafts and the subgrid column of environment, respectively.

As far as the interaction between the convective drafts and the environment is concerned, the top-hat profile approximation is used; that is, ψ is spatially homogeneous in each subgrid column. Also, the flux on the boundaries of the subgrid columns is more representative than the flux divergence within the subgrid columns, so the divergence theorem is applied to the integrals of flux density divergence in equation (A6):

$$\mathrm{SSS}_\psi\cong\frac{1}{V}\left[\sum_i\left(\Psi_i+\varepsilon_i\tilde{\psi}-\delta_i\psi_i-J_{it}\psi_{it}+J_{ib}\psi_{ib}\right)+\left(\tilde{\Psi}-\sum_i\varepsilon_i\tilde{\psi}+\sum_i\delta_i\psi_i-\tilde{J}_t\tilde{\psi}_t+\tilde{J}_b\tilde{\psi}_b\right)-\left(\overline{\Psi}-\overline{J_t}\,\overline{\psi_t}+\overline{J_b}\,\overline{\psi_b}\right)\right], \tag{A7}$$

where the variables are defined as follows: Ψ, sources or sinks; ε_i, entrainment rate; δ_i, detrainment rate; J, upward or downward vertical mass flow rate; subscript t, upper boundaries; and subscript b, lower boundaries. The three parentheses denote the local tendency of spatially integrated $\rho\psi$ in the ith convective draft, the environment, and the grid box, respectively. Note that the flux on the lateral boundary of the grid box has been canceled by that of the environment since the convective drafts contribute nothing here. Figure A1 is a

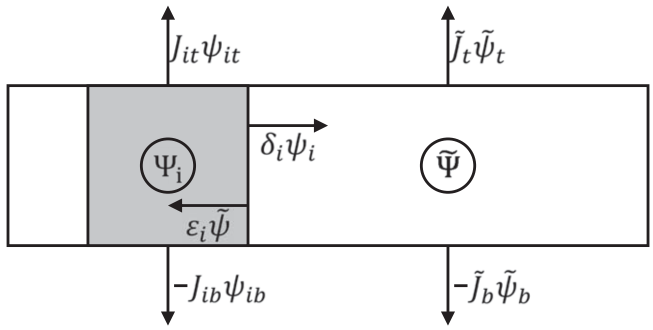

Figure A1. The schematic vertical cross section for equation (A7). The *i*th convective draft is filled with gray and is marked with subscripts *i* while the environment is filled with white and is marked with tildes. The circles denote sources or sinks, and the arrows denote mass-coupled ψ flux.

schematic diagram for the first two parentheses in equation (A7). All terms except sources or sinks are mass-coupled ψ flux, i.e., the mass flow rate multiplied by the ψ in the upstream or on the boundary. Since ε_i is the mass flow rate from the environment to the convective draft, it is multiplied by $\tilde{\psi}$. Oppositely, δ_i is the mass flow rate from the convective draft to the environment so is multiplied by ψ_i. Moreover, J is the vertical mass flow rate on the boundary so is multiplied by ψ on the boundary.

Equation (A7) is a general formulation of HYMACS. It considers SSS_ψ as the difference between the total and the ensemble average and treats the total with the ensemble-spatial-temporal average approximation and the top-hat profile approximation. Furthermore, considering σ, a weighted average equation, $\overline{\psi}=\sum_i \sigma_i\psi_i+\left(1-\sum_i \sigma_i\right)\tilde{\psi}$ could be applied to equation (A7).

A3. The Closure Assumptions for HY and KF

Then, KF uses other three assumptions in the following: the steady-state plume, the $\sigma \ll 1$, and the local compensation [*Kain*, 2004; *Kain and Fritsch*, 1990, 1993]. On the other hand, HY only uses the first two assumptions by eliminating the local compensation assumption.

The steady-state plume assumption means that the convective drafts remain in steady states within a characteristic time of convective adjustment. This sets the first parenthesis in equation (A7) to zero and yields:

$$\mathrm{SSS}_\psi \cong \frac{1}{V}\left[\left(\tilde{\Psi}-\sum_i \varepsilon_i\tilde{\psi}+\sum_i \delta_i\psi_i-\tilde{J}_t\tilde{\psi}_t+\tilde{J}_b\tilde{\psi}_b\right)-\left(\overline{\Psi}-\overline{J_t}\,\overline{\psi_t}+\overline{J_b}\,\overline{\psi_b}\right)\right], \tag{A8}$$

This assumption may not be a realistic approximation since it stops the convective drafts from changing until the characteristic time is over. However, it is acceptable in this study as far as a time scale not shorter than the characteristic time is concerned.

The $\sigma \ll 1$ assumption simplifies the weighted average equation to $\tilde{\psi}=\overline{\psi}$, treating the environment as the grid box. Applying this and $\tilde{J}=\overline{J}$ to equation (A8) yields the particular formulation of HY:

$$\mathrm{SSS}_\psi \cong \frac{1}{V}\sum\nolimits_i \left(-\varepsilon_i\overline{\psi}+\delta_i\psi_i\right), \tag{A9a}$$

which is equivalent to equations (11) and (12) in *Kuell et al*. [2007]. On the other hand, the local compensation applies $\tilde{J}=\overline{J}-\sum_i J_i$ and $\tilde{\psi}=\overline{\psi}$ to equation (A8) yields the particular formulation of KF:

$$\mathrm{SSS}_\psi \cong \frac{1}{V}\sum_i \left(-\varepsilon_i\overline{\psi}+\delta_i\psi_i+J_{it}\overline{\psi_t}-J_{ib}\overline{\psi_b}\right), \tag{A9b}$$

which is equivalent to equation (16.8) in *Kain and Fritsch* [1993]. Equation (A9a) means that SSS_ψ is the average effects of the following mass-coupled ψ flux: $-\varepsilon_i\overline{\psi}$, flux from the environment to the convective drafts; $\delta_i\psi_i$, flux from the convective drafts to the environment. In addition, equation (A9b) has the local compensation terms in the following: $J_{it}\overline{\psi_t}$, downward flux on the upper boundary of the environment compensating the convective updrafts, or upward one compensating the convective downdrafts; $-J_{ib}\overline{\psi_b}$, flux similar to $J_{it}\overline{\psi_t}$ but on the lower boundary.

The particular closures of HY and KF are done by two one-dimensional plume models diagnosing ε_i, δ_i, and ψ_i in equation (A9a) or also J_{it} and J_{ib} in equation (A9b); one with $i=u$ for convective updrafts, and the other with $i=d$ for convective downdrafts. In the mass compensation experiment, ε_i at the bottom of the prescribed updraft and δ_i at the top of it are set to a constant rate, which is accompanied with an upward mass flow rate, i.e., the mass lifting rate. On the other hand, HY and KF use the same plume models from KF, including the trigger function and the algorithm diagnosing ε_i, δ_i, and ψ_i, but use different formulations for SSS_ψ. In other words, from KF to HY, nothing is included or excluded until the final step, calculating SSS_ψ. Note that the local compensation is applied in the algorithm diagnosing convective drafts but is excluded from the final step. HY, with the dynamic compensation, has parameterized mass sources or sinks due to entrainment and detrainment in the convective drafts, which would be compensated with nonhydrostatic fully compressible model dynamics. On the other hand, KF, with the local compensation, has mass compensating flux in the environment which offsets the mass sources or sinks due to the convective drafts. Note that in WRF, KF calculates the SSS_ψ of potential temperature and moisture contents but not momentum, and so does HY. SSS_1 in HY might affect acceleration through the last two terms on the right hand side of $\frac{d\overline{\mathbf{V}}}{dt}=\frac{1}{\overline{\rho}}\frac{\partial\overline{\rho}\overline{\mathbf{V}}}{\partial t}+\overline{\mathbf{V}_\mathbf{h}}\cdot\nabla\overline{\mathbf{V}}+\overline{w}\frac{\partial\overline{\mathbf{V}}}{\partial z}-\frac{\overline{\mathbf{V}}}{\overline{\rho}}\frac{\partial\overline{\rho}}{\partial t}$, where $\mathbf{V_h}$ and w denote the horizontal and vertical components of velocity, respectively. However, the typical order of magnitude of these two terms are 10^{-3} m s^{-2}, which is significantly smaller than that of the horizontal advection term, 10^{-2} m s^{-2}. Also note that the trigger function from KF remains not changed once triggered until the convective adjustment is over, so the dynamic compensation cannot affect the trigger function in a timescale shorter than the adjustment.

A4. Mass Sources or Sinks in Terrain-Following Hydrostatic-Pressure Coordinate

HYMACS introduces mass sources or sinks to the mass continuity equation. For models with geometric height, z, as the vertical coordinate and with mass density as the prognostic variable for mass continuity equation, equation (A3) is straightforward. However, the Advanced Research WRF uses terrain-normalized hydrostatic pressure, η, as the vertical coordinate and uses pseudo density, $\overline{\mu}$, as the prognostic variable, so equation (A3) should be transformed to this coordinate following *Kasahara* [1974] and *Laprise* [1992]:

$$\overline{\mu}\equiv\frac{\partial\overline{\pi}}{\partial\eta}=-\overline{\rho}\,\frac{\partial\overline{\varphi}}{\partial\eta}, \tag{A10a}$$

$$\nabla_{\boldsymbol{z}}=\nabla_{\boldsymbol{\eta}}+\overline{\mu}^{-1}\overline{\rho}\left(\nabla_{\boldsymbol{\eta}}\overline{\varphi}\right)\frac{\partial}{\partial\eta}, \tag{A10b}$$

$$\frac{\partial}{\partial z}=-\overline{\mu}^{-1}\overline{\rho}g\,\frac{\partial}{\partial\eta}, \tag{A10c}$$

where the symbols are defined as follows: π, hydrostatic pressure; φ, geopotential; and g, acceleration due to gravity. Taking ψ as unity, applying equations (A10a) and multiplying $\frac{\overline{\mu}}{\overline{\rho}}$ make equation (A3):

$$\left(\frac{\partial\overline{\mu}}{\partial t}\right)_\eta+\nabla_{\boldsymbol{\eta}}\cdot\left(\overline{\mu}\overline{\mathbf{V}_\mathbf{h}}\right)+\frac{\partial}{\partial\eta}\left(\overline{\mu}\overline{\dot{\eta}}\right)=\frac{\overline{\mu}}{\overline{\rho}}SSS_1. \tag{A11}$$

Equation (A11) is used in the adapted version of WRF to calculate $\left(\frac{\partial\overline{\mu}}{\partial t}\right)_\eta$ and $\overline{\dot{\eta}}$ in this study; the left hand side is equivalent to equation (40) in *Laprise* [1992], but there are subgrid-scale mass sources or sinks, SSS_1, instead of zero on the right hand side.

A5. Subgrid-Scale Specific Enthalpy Forcing in Hydrostatic-Pressure Coordinate

Subgrid-scale specific enthalpy forcing includes heating and pressure work done, $\frac{1}{\overline{\rho}}\overline{\dot{P}}$, where P denotes pressure. The calculation is straight forward for heating but not for pressure work done because $\dot{\overline{P}}$ is a grid-scale process. Still, pressure work done by subgrid-scale mass flux could be estimated through hydrostatic-pressure work done, $\frac{1}{\overline{\rho}}\overline{\dot{\pi}}$. Following *Kasahara* [1974] and *Laprise* [1992]:

$$\overline{\rho}\,\frac{\partial\overline{\varphi}}{\partial\pi}=-1, \tag{A12a}$$

$$\nabla_{\boldsymbol{z}}=\nabla_{\boldsymbol{\pi}}+\overline{\rho}(\nabla_{\boldsymbol{\pi}}\overline{\varphi})\frac{\partial}{\partial\pi}, \tag{A12b}$$

$$\frac{\partial}{\partial z}=-\overline{\rho}g\,\frac{\partial}{\partial\pi}. \tag{A12c}$$

Taking ψ as unity, applying equations (A12a) and multiplying $\frac{1}{\overline{\rho}}$ make equation (A3):

$$\nabla_\pi \cdot \overline{\mathbf{V_h}} + \frac{\partial \bar{\tilde{\pi}}}{\partial \pi} = \frac{1}{\bar{\rho}} \mathrm{SSS}_1. \tag{A13}$$

Integrating equation (A13) by π' from $\pi'=0$ to a hydrostatic-pressure level π and multiplying $\frac{1}{\bar{\rho}}$ yield:

$$\frac{1}{\bar{\rho}}\bar{\tilde{\pi}} = \frac{1}{\bar{\rho}} \int_0^\pi \left(-\nabla_\pi \cdot \overline{\mathbf{V_h}} + \frac{1}{\bar{\rho}} \mathrm{SSS}_1 \right) d\pi', \tag{A14}$$

where the last term on the right hand side indicates the work done by subgrid-scale mass flux. For example, net subgrid-scale upward mass flux, which is equivalent to an upper mass source and a lower mass sink, does positive work on the levels between the source and the sink, and this will lift the levels in terms of local geopotential tendency:

$$\frac{\partial \bar{\varphi}}{\partial t} = g\bar{w} - \overline{\mathbf{V_h}} \cdot \nabla_\pi \bar{\varphi} + \frac{1}{\bar{\rho}} \bar{\tilde{\pi}}. \tag{A15}$$

An additional view comparing the grid-scale response to HY and KF is replacing $\bar{w}$ in equation (A15) with the assumptions applied in each scheme and considering a steady state in which local tendency and horizontal advection of $\bar{\varphi}$ are zero:

$$0 = g\tilde{w} + \frac{1}{\bar{\rho}} \int_0^\pi -\nabla_\pi \cdot \overline{\mathbf{V_h}} d\pi' + \left(\frac{1}{\bar{\rho}} \int_0^\pi \frac{1}{\bar{\rho}} \mathrm{SSS}_1 d\pi' \right), \tag{A16a}$$

$$0 = \left(g\tilde{w} + \frac{1}{\bar{\rho}} \int_0^\pi \frac{1}{\bar{\rho}} \mathrm{SSS}_1 d\pi' \right) + \frac{1}{\bar{\rho}} \int_0^\pi -\nabla_\pi \cdot \overline{\mathbf{V_h}} d\pi'. \tag{A16b}$$

Equation (A16a) is for HY while equation (A16b) is for KF. Terms in the parentheses are subgrid-scale processes while others are grid-scale ones. The net vertical mass flux with HY and KF are the same if and only if $\frac{1}{\bar{\rho}} \int_0^\pi -\nabla_\pi \cdot \overline{\mathbf{V_h}} d\pi'$ are the same. However, suggested by the results of the experiments in this study, the local compensation could induce secondary circulation with upper divergence and lower convergence, so $\tilde{w}$ should be less downward in the midlevel with KF than HY. Numerically, the advection due to $\tilde{w}$ in KF is calculated in the cumulus parameterization while that in HY is calculated in the model dynamics; the former uses a first-order numerical scheme while the latter uses a third-order one. Thus, even if $\tilde{w}$ was the same in each scheme, KF might cause larger numerical error. Nevertheless, this is minor since $\tilde{w}$ is different.

Acknowledgments
This work was jointly funded by Ministry of Science and Technology, Taiwan (grants MOST 104–2111–M–002–002–MY3, MOST 105–2119–M–002–035 and MOST 105–2111–M–002–002) and Office of Naval Research Global (grant NICOP N62909–15–1–2008). We thank the editors and the reviewers for careful thoughts and useful comments. We thank Taida Institute for Mathematical Sciences for computational resources. Computer codes are included in a supporting information file.

References

Arakawa, A. (2004), The cumulus parameterization problem: Past, present, and future, *J. Clim.*, *17*(13), 2493–2525, doi:10.1175/1520-0442(2004)017<2493:RATCPP>2.0.CO;2.

Arakawa, A., and C.-M. Wu (2013), A unified representation of deep moist convection in numerical modeling of the atmosphere. Part I, *J. Atmos. Sci.*, *70*(7), 1977–1992, doi:10.1175/JAS-D-12-0330.1.

Arakawa, A., J.-H. Jung, and C.-M. Wu (2011), Toward unification of the multiscale modeling of the atmosphere, *Atmos. Chem. Phys.*, *11*(8), 3731–3742, doi:10.5194/acp-11-3731-2011.

Beljaars, A. (1995), The parametrization of surface fluxes in large-scale models under free convection, *Q. J. R. Meteorol. Soc.*, *121*(522), 255–270, doi:10.1002/qj.49712152203.

Davis, C., and L. F. Bosart (2002), Numerical simulations of the genesis of Hurricane Diana (1984). Part II: Sensitivity of track and intensity prediction, *Mon. Weather Rev.*, *130*(5), 1100–1124, doi:10.1175/1520-0493(2002)130 < 1100:NSOTGO>2.0.CO;2.

Dyer, A., and B. Hicks (1970), Flux-gradient relationships in the constant flux layer, *Q. J. R. Meteorol. Soc.*, *96*(410), 715–721, doi:10.1002/qj.49709641012.

Emanuel, K., K. Oouchi, M. Satoh, H. Tomita, and Y. Yamada (2010), Comparison of explicitly simulated and downscaled tropical cyclone activity in a high-resolution global climate model, *J. Adv. Model. Earth Syst.*, *2*, 9, doi:10.3894/JAMES.2010.2.9.

Fritsch, J., and C. Chappell (1980), Numerical prediction of convectively driven mesoscale pressure systems, Part II. Mesoscale model, *J. Atmos. Sci.*, *37*(8), 1734–1762, doi:10.1175/1520-0469(1980)037<1734:NPOCDM>2.0.CO;2.

Gassmann, A. (2013), A global hexagonal C-grid non-hydrostatic dynamical core (ICON-IAP) designed for energetic consistency, *Q. J. R. Meteorol. Soc.*, *139*(670), 152–175, doi:10.1002/qj.1960.

Gentry, M. S., and G. M. Lackmann (2010), Sensitivity of simulated tropical cyclone structure and intensity to horizontal resolution, *Mon. Weather Rev.*, *138*(3), 688–704, doi:10.1175/2009MWR2976.1.

Grabowski, W. W. (2001), Coupling cloud processes with the large-scale dynamics using the cloud-resolving convection parameterization (CRCP), *J. Atmos. Sci.*, *58*(9), 978–997, doi:10.1175/1520-0469(2001)058 < 0978:CCPWTL>2.0.CO;2.

Grabowski, W. W. (2015), Untangling microphysical impacts on deep convection applying a novel modeling methodology, *J. Atmos. Sci.*, *72*(6), 2446–2464, doi:10.1175/JAS-D-14-0307.1.

Grabowski, W. W., and P. K. Smolarkiewicz (1999), CRCP: A cloud resolving convection parameterization for modeling the tropical convecting atmosphere, *Physica D*, *133*(1), 171–178, doi:10.1016/S0167-2789(99)00104-9.

Grell, G. A., and S. R. Freitas (2014), A scale and aerosol aware stochastic convective parameterization for weather and air quality modeling, *Atmos. Chem. Phys.*, *14*(10), 5233–5250, doi:10.5194/acpd-13-23845-2013.

Hong, S.-Y., Y. Noh, and J. Dudhia (2006), A new vertical diffusion package with an explicit treatment of entrainment processes, *Mon. Weather Rev.*, *134*(9), 2318–2341, doi:10.1175/MWR3199.1.

Houze, R. A., Jr. (2010), Clouds in tropical cyclones, *Mon. Weather Rev.*, *138*(2), 293–344, doi:10.1175/2009MWR2989.1.

Jordan, C. L. (1958), Mean soundings for the West Indies area, *J. Meteorol.*, *15*(1), 91–97, doi:10.1175/1520-0469(1958)015 < 0091:MSFTWI>2.0.CO;2.

Kain, J. S. (2004), The Kain-Fritsch convective parameterization: An update, *J. Appl. Meteorol.*, *43*(1), 170–181, doi:10.1175/1520-0450(2004)043 < 0170:TKCPAU>2.0.CO;2.

Kain, J. S., and J. M. Fritsch (1990), A one-dimensional entraining/detraining plume model and its application in convective parameterization, *J. Atmos. Sci.*, *47*(23), 2784–2802, doi:10.1175/1520-0469(1990)047 < 2784:AODEPM>2.0.CO;2.

Kain, J. S., and J. M. Fritsch (1993), Convective parameterization for mesoscale models: The Kain-Fritsch scheme, in *The Representation of Cumulus Convection in Numerical Models*, edited by K. A. Emanuel and D. J. Raymond, pp. 165–170, Am. Meteorol. Soc., Boston, doi:10.1007/978-1-935704-13-3_16.

Kasahara, A. (1974), Various vertical coordinate systems used for numerical weather prediction, *Mon. Weather Rev.*, *102*(7), 509–522, doi:10.1175/1520-0493(1974)102 < 0509:VVCSUF>2.0.CO;2.

Kessler, E. (1995), On the continuity and distribution of water substance in atmospheric circulations, *Atmos. Res.*, *38*(1), 109–145, doi:10.1016/0169-8095(94)00090-Z.

Kreitzberg, C. W., and D. J. Perkey (1977), Release of potential instability: Part II. The mechanism of convective/mesoscale interaction, *J. Atmos. Sci.*, *34*(10), 1569–1595, doi:10.1175/1520-0469(1977)034<1569:ROPIPI>2.0.CO;2.

Kuell, V., and A. Bott (2008), A hybrid convection scheme for use in non-hydrostatic numerical weather prediction models, *Meteorol. Z.*, *17*(6), 775–783, doi:10.1127/0941-2948/2008/0342.

Kuell, V., and A. Bott (2009), Application of the hybrid convection parameterization scheme HYMACS to different meteorological situations, *Atmos. Res.*, *94*(4), 743–753, doi:10.1016/j.atmosres.2009.04.002.

Kuell, V., A. Gassmann, and A. Bott (2007), Towards a new hybrid cumulus parametrization scheme for use in non-hydrostatic weather prediction models, *Q. J. R. Meteorol. Soc.*, *133*(623), 479–490, doi:10.1002/qj.28.

Laprise, R. (1992), The Euler equations of motion with hydrostatic pressure as an independent variable, *Mon. Weather Rev.*, *120*(1), 197–207, doi:10.1175/1520-0493(1992)120 < 0197:TEEOMW>2.0.CO;2.

Miyakawa, T., M. Satoh, H. Miura, H. Tomita, H. Yashiro, A. T. Noda, Y. Yamada, C. Kodama, M. Kimoto, and K. Yoneyama (2014), Madden–Julian Oscillation prediction skill of a new-generation global model demonstrated using a supercomputer, *Nat. Commun.*, *5*, 3769, doi:10.1038/ncomms4769.

Molinari, J., and M. Dudek (1992), Parameterization of convective precipitation in mesoscale numerical models: A critical review, *Mon. Weather Rev.*, *120*(2), 326–344, doi:10.1175/1520-0493(1992)120 < 0326:POCPIM>2.0.CO;2.

Park, S. (2014), A unified convection scheme (UNICON). Part I: Formulation, *J. Atmos. Sci.*, *71*(11), 3902–3930, doi:10.1175/JAS-D-13-0233.1.

Paulson, C. A. (1970), The mathematical representation of wind speed and temperature profiles in the unstable atmospheric surface layer, *J. Appl. Meteorol.*, *9*(6), 857–861, doi:10.1175/1520-0450(1970)009 < 0857:TMROWS>2.0.CO;2.

Rotunno, R., and K. A. Emanuel (1987), An air-sea interaction theory for tropical cyclones. Part II: Evolutionary study using a nonhydrostatic axisymmetric numerical model, *J. Atmos. Sci.*, *44*(3), 542–561, doi:10.1175/1520-0469(1987)044 < 0542:AAITFT>2.0.CO;2.

Rozoff, C. M., D. S. Nolan, J. P. Kossin, F. Zhang, and J. Fang (2012), The roles of an expanding wind field and inertial stability in tropical cyclone secondary eyewall formation, *J. Atmos. Sci.*, *69*(9), 2621–2643, doi:10.1175/JAS-D-11-0326.1.

Schubert, W. H., and J. J. Hack (1982), Inertial stability and tropical cyclone development, *J. Atmos. Sci.*, *39*(8), 1687–1697, doi:10.1175/1520-0469(1982)039 < 1687:ISATCD>2.0.CO;2.

Singh, K. S., and M. Mandal (2014), Sensitivity of mesoscale simulation of Aila Cyclone to the parameterization of physical processes using WRF Model, in *Monitoring and Prediction of Tropical Cyclones in the Indian Ocean and Climate Change*, edited by U. C. Mohanty et al., pp. 300–308, Springer Netherlands, Dordrecht, doi:10.1007/978-94-007-7720-0_26.

Skamarock, W., J. Klemp, J. Dudhia, D. Gill, D. Barker, M. Duda, X. Huang, W. Wang, and J. Powers (2008), A description of the advanced research WRF Version 3, *NCAR Tech. Note NCAR/TN-475+STR*, Natl. Cent. for Atmos. Res., Boulder, Colo., doi:10.5065/D68S4MVH.

Skamarock, W. C., J. B. Klemp, M. G. Duda, L. D. Fowler, S.-H. Park, and T. D. Ringler (2012), A multiscale nonhydrostatic atmospheric model using centroidal Voronoi tesselations and C-grid staggering, *Mon. Weather Rev.*, *140*(9), 3090–3105, doi:10.1175/MWR-D-11-00215.1.

Srinivas, C., R. Venkatesan, D. B. Rao, and D. H. Prasad (2007), Numerical simulation of Andhra severe cyclone (2003): Model sensitivity to the boundary layer and convection parameterization, in *Atmospheric and Oceanic Mesoscale Processes*, edited by M. Sharan and S. Raman, pp. 1465–1487, Birkhäuser Basel, Basel, Switzerland, doi:10.1007/978-3-7643-8493-7_3.

Sun, Y., L. Yi, Z. Zhong, Y. Hu, and Y. Ha (2013), Dependence of model convergence on horizontal resolution and convective parameterization in simulations of a tropical cyclone at gray-zone resolutions, *J. Geophys. Res. Atmos.*, *118*, 7715–7732, doi:10.1002/jgrd.50606.

Webb, E. K. (1970), Profile relationships: The log-linear range, and extension to strong stability, *Q. J. R. Meteorol. Soc.*, *96*(407), 67–90, doi:10.1002/qj.49709640708.

Wu, C.-M., and A. Arakawa (2014), A unified representation of deep moist convection in numerical modeling of the atmosphere. Part II, *J. Atmos. Sci.*, *71*(6), 2089–2103, doi:10.1175/JAS-D-13-0382.1.

Yamada, Y., K. Oouchi, M. Satoh, H. Tomita, and W. Yanase (2010), Projection of changes in tropical cyclone activity and cloud height due to greenhouse warming: Global cloud-system-resolving approach, *Geophys. Res. Lett.*, *37*, L07709, doi:10.1029/2010GL042518.

Zhang, D., and R. A. Anthes (1982), A high-resolution model of the planetary boundary layer-sensitivity tests and comparisons with SESAME-79 data, *J. Appl. Meteorol.*, *21*(11), 1594–1609, doi:10.1175/1520-0450(1982)021 < 1594:AHRMOT>2.0.CO;2.

Zheng, Y., K. Alapaty, J. A. Herwehe, A. D. Del Genio, and D. Niyogi (2016), Improving high-resolution weather forecasts using the Weather Research and Forecasting (WRF) Model with an updated Kain–Fritsch scheme, *Mon. Weather Rev.*, *144*(3), 833–860, doi:10.1175/MWR-D-15-0005.1.

Erratum

In the originally published version of this article there were errors in Table 1. The first row in the 3rd and 4th columns included “hPa” erroneously. In these instances, “hPa” should have been published as “Pa” This error has since been corrected, and this version may be considered authoritative version of record.